A Concentric Tube Steerable Drilling Robot for Minimally Invasive Spinal Fixation of Osteoporotic Vertebrae

A Concentric Tube Steerable Drilling Robot for Minimally Invasive Spinal Fixation of Osteoporotic Vertebrae

Susheela Sharma[1], Tarunraj G. Mohanraj[1], Jordan P. Amadio[2], Mohsen Khadem[3], and Farshid Alambeigi[1], *Member, IEEE* .

***Abstract*— Spinal fixation with rigid pedicle screws have shown to be an effective treatment for many patients. However, this surgical option has been proved to be insufficient and will eventually fail for patients experiencing osteoporosis. This failure is mainly attributed to the lack of dexterity in the existing rigid drilling instruments and the complex anatomy of vertebrae, forcing surgeons to implant rigid pedicle screws within the osteoporotic regions of anatomy. To address this problem, in this paper, we present the design, fabrication, and evaluation of a unique flexible yet structurally strong concentric tube steerable drilling robot (CT-SDR). The CT-SDR is capable of drilling smooth and accurate curved trajectories through hard tissues without experiencing buckling and failure; thus enabling the use of novel flexible pedicle screws for the next generation of spinal fixation procedures. Particularly, by decoupling the control of bending and insertion degrees of freedom (DoF) of the CT-SDR, we present a robotic system that (i) is intuitive to steer as it does not require an on-the-fly control algorithm for the bending DoF, and (ii) is able to address the contradictory requirements of structural stiffness and dexterity of a flexible robot interacting with the hard tissue. The robust and repeatable performance of the proposed CT-SDR have been experimentally evaluated by conducting various drilling procedures on simulated bone materials and animal bone samples. Experimental results indicate drilling times as low as 35 seconds for curved trajectories with 41 mm length and remarkable steering accuracy with a maximum 2% deviation error.**

***Index Terms*— Medical Robots and Systems, Steerable Drilling Robot, Minimally Invasive Spinal Fixation Procedure.**

I. Introduction

Osteoporosis is a serious public health concern, described as a generalized decrease in bone mineral density (BMD) by more than 2.5 standard deviations below the healthy population mean [1], [2]. Osteoporosis is responsible for an estimated

*This work is supported by the National Institute Of Biomedical Imaging and Bioengineering of the National Institutes of Health under Award Number R21EB030796.

S. Sharma, T. G. Mohanraj, and F. Alambeigi are with the Walker Department of Mechanical Engineering and Texas Robotics at the University of Texas at Austin, Austin, TX, 78712, USA. Email: { sheela.sharma, tarunrajgm}@utexas.edu, farshid.alambeigi @austin.utexas.edu

J. P. Amadio is with the Department of Neurosurgery, The University of Texas Dell Medical School, TX, 78712.

M. Khadem is with the School of Informatics, University of Edinburgh, UK.

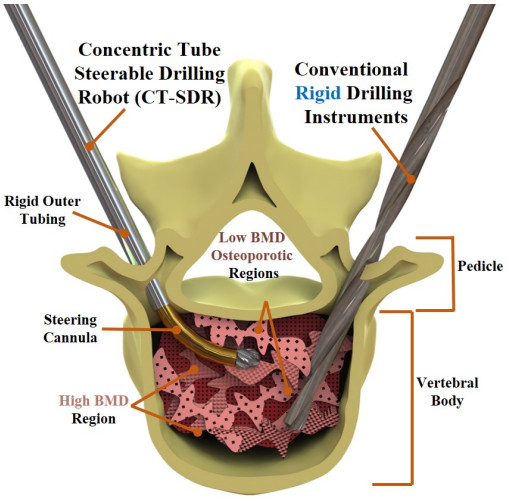

Fig. 1: Conceptual illustration of the proposed CT-SDR, drilling a J-shape trajectory through the pedicle toward high BMD regions of an L3 vertebra compared with a conventional rigid drilling instrument constrained to linear trajectories. As shown, the proposed CT-SDR is composed of a stationary rigid outer tubing and a pre-curved steering cannula. Of note, the figure presents the cross section of a vertebra cut across its axial plane, together with the conceptual high and low BMD regions within an osteoporotic vertebral body.

2 million broken bones per year in the United States [3], [4]. Of these osteoporotic fractures, vertebral compression fractures are the most common type (about 47%) with more than 1.4 million global incidence in men and women over age 50 [5]. In fractures too unstable for nonsurgical methods (e.g., medications and orthotic bracing), patients may require a spinal fusion surgery. In this intervention, with the goal of internal fixation of the spine, two (or more) vertebrae are locked together using rigid pedicle screws so that they can fuse into one solid bone, eliminating painful motion and restoring stability to the spine. This same procedure is also commonly performed in elective fusion operations for degenerative spine disease, which predominantly affects older adults and frequently co-occurs with osteoporosis [6].

Despite the well-established benefits of a fusion procedure, for an osteoporotic vertebral body, stability of fusion with rigid screws is often insufficient and the fixation may fail [7]–[9].

As conceptually shown in Fig. 1, this failure can mainly be attributed to the lack of dexterity in existing rigid drilling instruments, linear trajectory of the rigid pedicle screws, and the complex anatomy of vertebra forcing the surgeon to implant the screw within low BMD osteoporotic regions [10]. Using novel flexible drilling instruments, surgeons would be able to access new areas of the vertebra, including high BMD regions (shown in Fig. 1), for placement of bendable pedicle screws, (e.g., the ones proposed in [11], [12]) thus improving the quality of spinal fixation surgeries. This demands a flexible yet structurally strong robot/instrument that is able to accurately, robustly, and quickly drill a pre-planned smooth curved path into a patient's hard tissue (bone) without disrupting the surgeon's procedural workflow [12], [13].

Providing a simultaneous balance between the structural stiffness and dexterity of a flexible drilling robot while drilling a pre-planned smooth curved path is the essential challenge in designing these robotic systems [12], [14]. Of note, this design requirement is of considerable importance to avoid buckling and drilling failure when external interaction forces are exerted on the robotic system [15], [16]. To overcome the aforementioned challenges, literature documents a few flexible drilling robots developed to improve clinicians' access within hard tissues. For instance, Alambeigi et al. [12], [13] utilized a tendon-driven continuum manipulator to develop a robotic system capable of drilling relatively smooth curved holes for treatment of femoral head osteonecrosis. The proposed system, however, suffers from several limitations including a lengthy drilling procedure, as long as 5-9 minutes, for cutting a small curved path with a maximum 35 mm length. This is mainly due to the lack of adequate structural stiffness and inherent compliance of the utilized continuum manipulator, increasing the risk of drilling failure and buckling at high insertion speeds [15]. More importantly, due to the high-compliance of tendon-driven continuum manipulators, this system is susceptible to early buckling and unable to be steered along an arbitrary pre-planned drilling trajectory [16]. The performed experiments by the authors solely demonstrated the feasibility of drilling a few curved trajectories based on predetermined drilling parameters (i.e., insertion and rotational speeds and actuation tensions). In other words, the parameters of the proposed tension-based control algorithm are tuned based on off-line drilling experiments that cannot be used on an arbitrary hard tissue with unknown mechanical properties. To partially address these limitations, recently, Ma et al. [17] developed a handheld version of the mentioned robotic system. Nevertheless, similar to the previous study, stiffness and bending behavior of the drilling robot are limited to the stiffness of the utilized continuum manipulator and the maximum loading capacity of the actuation tendons. Moreover, due to the inherent compliance and under-actuation of tendon-driven continuum manipulators, steering of this handheld drilling system (i.e., simultaneous control of insertion and bending Degrees-of-Freedom (DoF)) is highly unintuitive, as it requires a real-time control algorithm and embedded sensors to ensure accuracy of the steerable drilling. In an effort toward addressing the above-mentioned limitations, Wang et al. [16], [18] have recently proposed an actively controlled tendon-driven articulated surgical drilling system

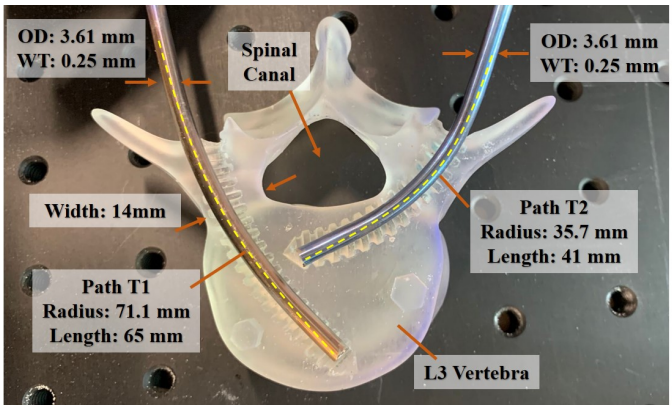

Fig. 2: A 3D printed L3 vertebra with two pre-defined desired J-shape drilling trajectories passing through the pedicles access region to the vertebral body. The figure also shows two NiTi Tubes heat treated based on these trajectories serving as the steering cannula for the CT-SDR.

for spinal fixation interventions. Although, compared to the conventional rigid drilling instruments, this drill grants more access to the areas within the vertebra, it does not allow for a smooth curved trajectory through the bone for implantation of bendable pedicle implants. In other words, due to the use of a rigid shaft and an articulated wrist/hinge, the drilled trajectory is restricted to multi-segment straight/linear paths into the bone.

With the goal of enhancing fusion stability in an osteoporotic vertebra, avoiding a spinal fixation failure, and inspired by Concentric Tube Robots (CTRs) (e.g., [19]–[22]), in this paper, we propose developing a unique, intuitive, and easy-to-control concentric tube steerable drilling robot (CT-SDR). A review of the literature (e.g., [14], [21]–[24]) demonstrates that in almost all of the use cases, (i) CTRs have been used for surgical interventions that either interacts with or avoids an interaction with a deformable/soft tissue (e.g., [14], [25]); (ii) CTRs' outer diameter often have been $<$2-3 mm that can be easily deformed by a light interaction with the environment leading them to be of poor use in applications in which interactions with hard tissues are required (e.g., [14], [24]); and (iii) CTRs demand real-time control techniques to steer the robot inside cavities and avoid interaction with the environment to ensure that their considered model is valid and the robot can be accurately controlled (e.g., [14], [26]). Nevertheless, as our main contributions and as opposed to CTRs, the proposed CT-SDR (i) has been designed to directly interact with a hard tissue, and indeed drill through it while accurately following a pre-defined drilling trajectory, without any failure and buckling; (ii) demands completely different design requirements such as a larger diameter for tubes and structurally strong mechanism to ensure accurately following the pre-defined drilling trajectory without experiencing failure; and (iii) does not require a real-time steerability control algorithm to ensure the manipulator is following the desired drilling trajectory. This unique feature is enabled through decoupling the bending and insertion DoFs providing a control-free, intuitive, and easy-to-steer system, similar to the conventional surgical drills with rigid drill bits. To our

knowledge, this application of CTRs for steerable drilling through a hard tissue (i.e., the vertebra) is the first of its kind. In this study, to thoroughly evaluate the performance, robustness, and repeatability of the proposed CT-SDR, we performed different drilling experiments on simulated bone materials and animal bone samples and quantitatively assessed the obtained drilling trajectories.

II. Design and Fabrication of the CT-SDR

To meet the needs discussed in the previous section, the spinal fixation CT-SDR should possess (i) flexible components that allow for adequate bending capability to cover areas within the vertebral body; (ii) power transmission from the actuator to the cutting instrument around a curve trajectory, (iii) sufficient structural stiffness to reliably interact with hard tissue to apply cutting forces; and (iv) flexible drilling instruments to reliably and quickly drill through hard tissues. To address these design requirements, the following sections will cover in detail the components of the proposed CT-SDR (i.e., the steering cannula, flexible cutting instruments, and the actuation unit) and how they are beneficial to the system as a whole as well as the manufacturing decisions that were included in the design.

A. The Concentric Tubes as the Steering Cannula

To provide simultaneous flexibility and structural strength for the CT-SDR, inspired by the design of concentric tube robots (e.g., [20]–[22]), we propose utilizing two concentric tubes including one outer rigid, straight stainless steel tubing and one inner, pre-curved, superelastic NiTi tubing. As shown in Fig. 1and Fig. 4, the outer tube is static while the superelastic NiTi tube is able to act as a steering cannula and house flexible cutting tools. Of note, NiTi as a superelastic, biocompatible, shape memory alloy is comprised of nickel and titanium and being used with a growing frequency for medical technologies and instruments [27]. When assembled, and the NiTi is fully within the stainless steel, it is constrained to the straight geometry of the stronger outer stainless steel tube. As the inner NiTi cannula is pushed forward out of the stainless steel tube, it returns to its pre-defined heat treated shape as shown in the subfigures of Fig. 4-II. The cutting tool is simultaneously guided by the cannula to follow the path dictated by the NiTi shape, along the planned drilling trajectory and not deviating from it. To achieve this, obtaining the correct dimensions for the NiTi tube and its heat treatment plays the largest role in the manufacturing of the CT-SDR. Additionally, for performing a spinal fixation procedure using the proposed CT-SDR, the desired drilling trajectory as well as the diameter and length of the drilling tunnel are critical and needs to be determined before the surgery (see Fig. 2). Of note, selection of these parameters depends on the BMD of the vertebral body (defining the level of osteoporosity of the patient), clinician's opinion, and geometry of the vertebral level (particularly, size of the pedicle width and vertebral body).

Considering the above-mentioned design criteria, to manufacture the desired drilling trajectory using a NiTi tube,

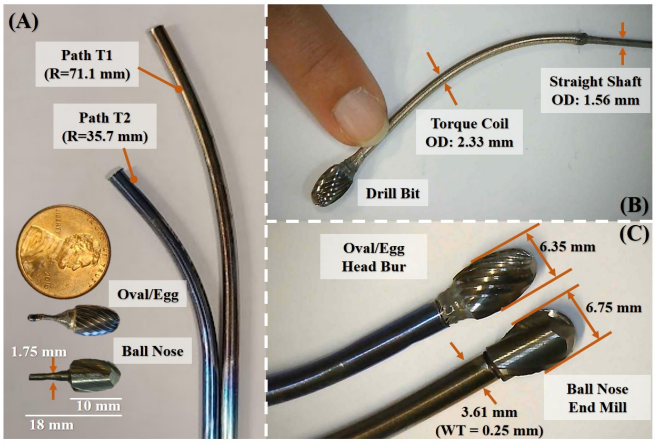

Fig. 3: (A) The flexible steering cannula (T1= 71.1 mm radius and T2= 35.7 mm radius). The figure also displays the drill bits prior to insertion into the torque coil. Both bits have a head length of 10 mm, an overall length of 18 mm, and a shank diameter from 1.5-2 mm when moving from tip towards the head; (B) The flexible cutting tool composed of a rounded drill bit at the distal end, a torque coil in the middle, and a straight rigid shaft at the proximal end of the tool adhered to each other; (C) A close view of the profile of the utilized drill bits and their cutting diameters.

it needs to be heat treated in a furnace while being constrained to the desired shape within a custom CNC-fabricated stainless steel jig. To design such a jig and without loss of generality, in this paper, we first arbitrarily chose an L3 vertebal model (shown in Fig. 2) and considered two curved trajectories with extreme radii of curvature of 35 mm and 69.5 mm, as the desired curved trajectories for heat treatment and drilling. Of note, successful heat treatment and drilling along with these two trajectories ensure that any intermediate curvatures/trajectories can also be successfully selected for these purposes. After selecting the desired drilling trajectory and before the heat treatment procedure, we next checked whether a NiTi tube can obtain this desired shape without experiencing plastic deformation and failure. To ensure this, the following equation was used to determine the minimum achievable midline radius of curvature r_{min} (shown in Fig. 5-C) before the material plastically deforms or fails [14], [28]:

$$r_{min} = \frac{D}{2}(1 + \frac{1}{\epsilon}) \tag{1}$$

where, D denotes the outer diameter of the NiTi tube and ϵ is the maximum strain of the NiTi (i.e., $\epsilon = 8\%$ or 0.08 [28]).

For the considered L3 vertebra with 14 mm pedicle width [29], [30], to ensure not compromising the nerves passing through spinal canal, we are interested in minimizing the chosen outer diameter for the NiTi tube. Therefore, considering this factor, the available NiTi tubes in the market, and the flexible cutting tool dimensions, we selected a NiTi with outer diameter of 3.61 mm. Using (2), a minimum achievable midline radius of curvature (r_{min}= 24.36 mm) was obtained that is smaller than the considered radius of curvatures for L3 vertebra (see Fig. 2) and theoretically ensures a successful superelastic performance without failure for both heat treated

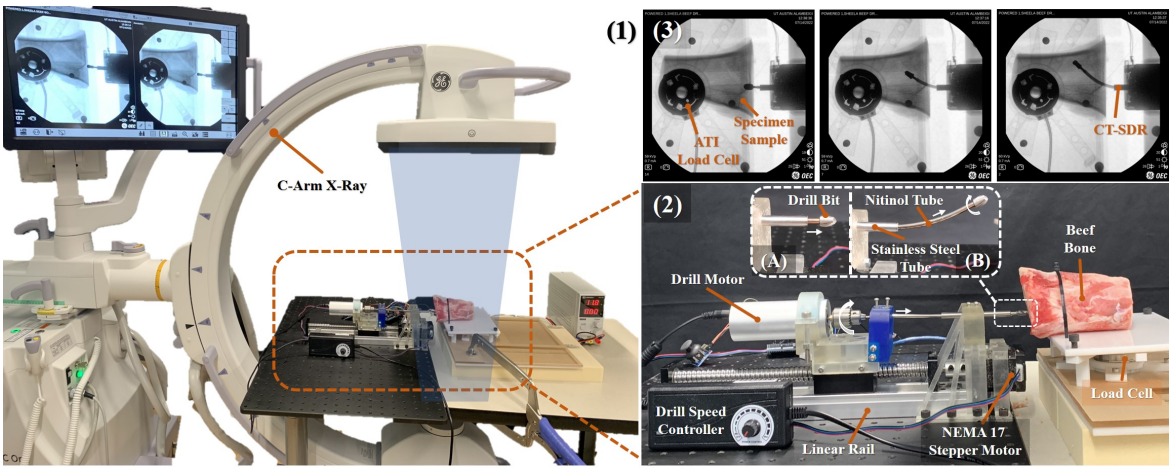

Fig. 4: Experimental set-up used to evaluate the performance of the CT-SDR including a C-arm X-ray machine, a six axis force/torque load cell, an animal bone test sample, and a holding mechanism. An overview of the full set-up is shown in (1) with the C-arm's visual cone depicted. Subfigure (2) gives a closer view of the CT-SDR system and the concentric tube actuation in (A) and (B). Subfigure (3) displays the view from the C-arm at the beginning, middle, and end of the drilling procedure on the animal bone sample. This view also shows the utilized six axis force/torque load cell mounted under the holding mechanism.

tubes. Finally, we followed the heat treatment instruction provided in previous studies (e.g., [31]) to perform this process. Figure 2 shows the heat treated NiTi tubes versus a 3D printed model of the considered L3 vertebral model and selected drilling trajectories. It is worth emphasizing that, tubes with these curvatures would grant a surgeon access to areas within the vertebral body that are not currently accessible with existing rigid instruments. The heat treated tubes are also shown together in Fig. 3-A. It is worth highlighting that the aforementioned design and heat treatment process is generic and the curvature of an NiTi tube can readily be changed and heat treated to provide the required access to the area of interest inside the vertebral body and any level of vertebra while satisfying (1).

For the CT-SDR presented in this paper, a singular 70 mm long, heat treated NiTi tube is nested within a straight stainless steel tube (89895K421, McMaster-Carr) with an identical length and 1.25 mm wall thickness. Compared to the typical concentric tube robots, the proposed CT-SDR uses a NiTi tube with larger diameter and wall thickness to provide more structural stiffness for the drilling system (i.e., outer diameter of OD = 3.61 mm and a wall thickness of WT = 0.25 mm) (Euroflex GmbH, Germany). As shown in Fig. 3, after heat treatment, the tubes held the planned radii of curvature while maintaining the superelastic properties originally sought after. To minimize the amount of NiTi tube used in the system and provide the adequate length for housing the flexible cutting tools, the NiTi tube is attached to a straight stainless steel tube (89895K712, McMaster-Carr) with 80 mm length and 3.175 mm outer diameter. This stainless steel tube is attached to the linear stage mechanism to advance and retract the NiTi tube. It is worth mentioning that the tube's OD and length can readily be changed depending on the vertebral geometry and pedicle dimension.

B. The Flexible Cutting Tool

As shown in Fig. 3, each flexible cutting tool is composed of a rounded drill bit at the distal end, a torque coil in the middle, and a straight rigid shaft at the proximal end of the tool adhered to each other using epoxy (1813A243, McMaster-Carr). To investigate the influence of the drill bit geometry on the cutting performance of the CT-SDR, two drill bits were selected and tested during the experimentation step including a carbide oval/egg head bur (42955A35, McMaster-Carr) and a ball nose end mill (8878A42, McMaster-Carr). Of note, both of these geometries have the capability to cut not only in the forward direction but also with the sides of the cutting tool making them promising choices for a tool that needs to cut in non-linear trajectories [13]. Both of these tools were ground down to have a shank diameter between 1.5-2 mm and given a slight taper to accommodate for the added torque coil. The heads of both the oval head and ball end mill were 10 mm in length, the shanks 8 mm in length, and had cutting tip diameters of 6.35 mm and 6.75 mm, respectfully. Both of these tools' geometries are shown in Fig. 3.

Also, as shown in Fig. 3, the drill bit at the distal end and the rigid shaft at the proximal end of the tool were separated by a torque coil with 70 mm length (Asahi Intec. USA, Inc.), designed to be fed through the NiTi cannula and transmit the provided rotational torque by the motor to the drill bit. So as to not crush/damage the torque coil and have a higher torque transmission efficiency, the straight rigid shaft was designed to be gripped by the chuck of the motor. For the oval head bur, the rigid shaft was a stainless steel rod (888915K11, McMaster-Carr) with a diameter of 1.56 mm whereas the ball end mill had a brass tube (8859K231, McMaster-Carr), with the same diameter, allowing to include a material removal or cooling mechanism with water or air being added to the cutting area through the inside of this innermost component.

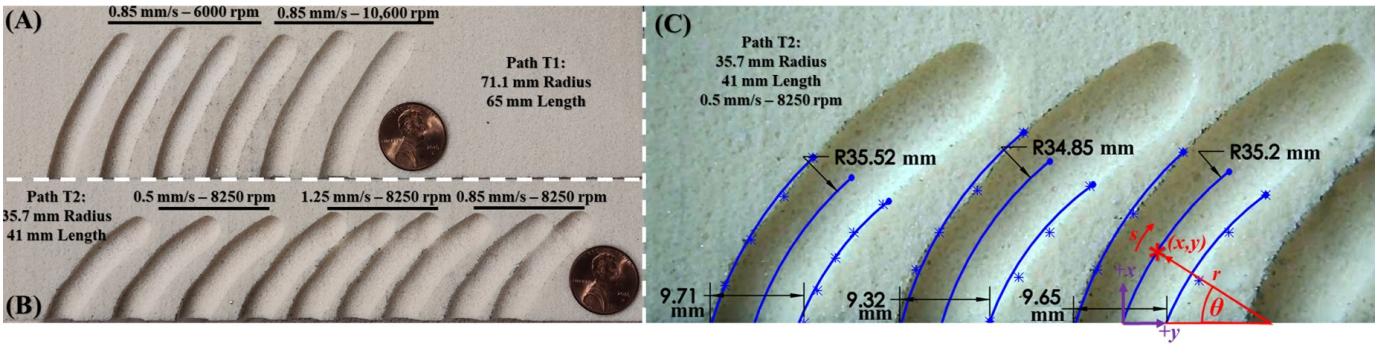

Fig. 5: A cross sectional view of some of the drilling experiments performed on Sawbone samples. (A) View of Path T1 tests with different rotational drilling speeds while the insertion speed of the CT-SDR was held at a constant 0.85 mm/s. (B) A view of Path T2 tests with variable insertion speeds while rotational drilling speed was held at a constant 8250 rpm. (C) This image depicts analysis of the drilling trajectories (i.e., radius of curvature and diameters of the drilled trajectories) obtained with the 35.7 mm radius NiTi curvature along with depicted variables used for calculations. All measurements are made in mm.

C. The Actuation Unit

The actuation unit, shown in Fig. 4, consists of one NEMA 17 stepper motor and linear stage with a linear ball screw (B085TG12D1, Amazon) to provide the insertion DoF, a mini electric handheld drill (B075SZZN4J, Amazon) that provides the required rotational speed and cutting torque for the flexible instrument, and 3D resin printed supports and mounts. The stepper motor was controlled with an Arduino Uno R3 microcontroller board and a custom-written program controlling the linear speed of the motor. The rotational speed of the motor was also set using the provided controller of the mini handheld drill. The design of the actuation unit is centered around the alignment of the tubes involved in the CT-SDR and the force required to to push forward or retract the NiTi cannula inside the other stainless steel tube. To overcome the friction present between the concentric tubes and to provide the force required to bend the NiTi tubes from their heat treated shape, the CT-SDR required a motor that could provide the appropriate amount of torque without weighing down the system and while maintaining a compact size. The NEMA 17 stepper motor not only allowed for a compact system but also for precise control during experimentation. The 3D printed parts added rigid supports to the system to resist internal friction forces, allowing for the continued alignment of the concentric tubes and creating a strong base for the motor to push against.

III. Evaluation Experiments and Results

A. Experimental Set-Up

In an operating room setting, a surgeon would align the surgical drill with the vertebra and slowly advance the drill in to cut the material and then back the mechanism straight out, while monitoring the accuracy and safety of the procedure using intermittent fluoroscopic images. This situation was replicated using the experimental setup shown in Fig. 4 designed to validate the concept of utilizing the CT-SDR for spinal fixation procedures. In the first set of experiments, Sawbone bio-mechanical bone model phantoms (block 10 PCF, Pacific Research Laboratories, USA) were used to simulate human bone with medium osteoporosis [32] before being replaced by animal bone samples in the later experiments [13]. The CT-SDR was mounted to an optical breadboard with the test sample held in front of the system. To visualize the interior of the test sample during testing, a C-arm X-ray machine (OEC One CFD, GE Healthcare) was set up perpendicular to the cutting plane. As the CT-SDR was actuated through the test sample, the C-arm was able to show the location of the drill tip and steering cannula and cutting trajectory throughout the experiments. This allowed us to monitor and see the experiment in real time and for a second avenue of analysis after the test's conclusion. As shown in Fig. 4, to measure the drilling forces imparted on the test specimen by the CT-SDR during each test, a six DOF force/torque load cell (Mini45, ATI Industrial Automation) was also added to the set-up and sample holder. An additional camera was also set up separate from the other components to track overall cutting time and closely monitor, externally, the performed experiments. Recorded videos of the performed experiments with these visuals have been provided in the complementary uploaded media file.

B. Sawbone Drilling Experiments

Every experiment run with the CT-SDR was to evaluate the system's performance in regards to the system requirements mentioned in Section II. Particularly, drilling time and repeatability/predictability of the resulting drilled tunnel (i.e., tunnel curvature), drilling force, the structural strength, buckling, and potential failure modes of the steering cannula together with the cutting performance of the drilling instruments were thoroughly investigated. Similar to the previous studies [13], [16], [17], several factors were determined to have potential effects on the system during initial experiments with the CT-SDR: (1) the insertion speed of the steering cannula, (2) the rotational speed of the cutting instrument, and (3) the drill tip geometry. To this end, we performed two different types of experiments with the two heat treated NiTi cannulas and the drilling instruments as follows:

1) J-shape Axial-Plane Drilling tunnels: We first evaluated the performance of the CT-SDR by simulating a scenario in which a J-shape tunnel is drilled across the axial plane of a vertebra, similar to the one shown in Fig. 1. To this end, after performing preliminary experiments, it was determined that the three insertion speeds to be considered during ex-

TABLE I: Experimental data from the repeatability tests done with the oval head bur tool and the 71.1 mm radius NiTi tube. The table summarizes the average radii from each test set, the standard deviation of the test set, the % difference between the average value and the actual radius of curvature of the NiTi tube, and the average time it took to drill the paths.

Insert Setting - Drill Setting [mm/s]-[rpm]	Average Radius [mm]	Standard Deviation	% Difference From Actual	Time [s]
1.25-8250	69.9	0.43	1.7	43.7
0.5-8250	69.8	0.59	1.9	102.3
0.85-10600	69.8	0.63	1.9	59
0.85-6000	69.9	0.41	1.76	59
0.85-8250	69.6	0.26	2.15	59

TABLE II: Experimental data from the repeatability tests done with the oval head bur tool and the 35.7 mm radius NiTi tube. The table summarizes the average radii from each test set, the standard deviation of the test set, the % difference between the average value and the actual radius of curvature of the NiTi tube, and the average time it took to drill the paths.

Insert Setting - Drill Setting [mm/s]-[rpm]	Average Radius [mm]	Standard Deviation	% Difference From Actual	Time [s]
1.25-8250	37.1	1.03	4.1	35
0.5-8250	34.9	0.30	2.0	81
0.85-10600	35.6	0.55	0.14	49.3
0.85-6000	35.2	0.57	1.3	49.3
0.85-8250	35.1	0.80	1.57	49.3

perimentation would be 0.5, 0.85, and 1.25 mm/s, and the three rotational drill speeds would be 6000, 8250, and 10600 rpm. Five different trials were run for each of the NiTi tubes heat treated for this project with each trial being repeated 3 times. A total of 30 tests performed in all with the oval head drill tip. Of note, in these experiments, we fixed the bending plane of the NiTi cannula to be parallel with the optical table to represent drilling parallel to the axial plane. After the main experiments were concluded, the ball nose end mill was also tested with both NiTi steering cannula, insertion speeds of 0.85 mm/s and 1.25 mm/s, and a drilling speed of 8250 rpm. As opposed to the experiments performed in [13] demanding a pilot hole to introduce the drill in the material, in each trial, the drilling started without a pilot hole or starting assistance of any kind, and was simply advanced into the flat face of the test sample. This replicates the starting conditions of a vertebral insertion drilling in which, in real surgical scenarios, the surface is first flattened for easier insertion. In each trial, the drill was advanced the full length of the respective heat treated NiTi cannula used in that trial, while the C-arm (intermittently) and external camera (continuously) were recording the experimental procedure. After the trials were completed, videos were taken of the interior of each trial using a 5.5 mm Borescope Camera (TELESION Inc., China) inserted through the drill's entrance hole to qualitatively assess the curvatures and internal smoothness of each pathway. Next, the samples were cut along the mid-line of the entrance holes, and were closely inspected and photographed using a digital microscope (Jiusion, China). The images were then analyzed with a 3D CAD software (SolidWorks, Dassault Systèmes) to determine each path's radius of curvature and compared to the ideal and the actual radii of the NiTi tubes. Figure 5 displays the cross sectional views of some of the repeated drilled trajectories and the analyzed view of one of the tests completed with the trajectory T2 (35.7 mm NiTi cannula). Also, Fig. 6 represents an exemplary planar J-shape trajectory drilled with the CT-SDR. The entry and exit points are on faces 90 degree angle from one another. For this trial, the CT-SDR was set to 0.85 mm/s insertion, 8250 rpm drill speed, and was aligned perpendicular to the entry face while proceeded to drill along the T1 path. Tables I and II summarize the results of the performed experiments with respect to the drilling time

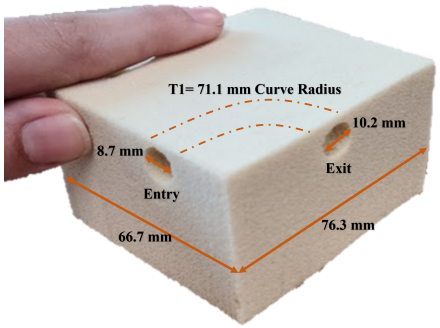

Fig. 6: An exemplary planar J-shape trajectory drilled with the CT-SDR. The entry and exit points are on faces 90 degree angle from one another. The CT-SDR was set to 0.85 mm/s insertion, 8250 rpm drill speed, and was aligned perpendicular to the entry face. The CT-SDR proceeded to drill along the T1 path.

and repeatability (i.e., drilled tunnel radius of curvature) of the performed trials with both NiTi cannulas. The results of the performed experiments were also compiled into Fig. 9, which shows the comparison of the average measured and the desired drilling trajectories of the 30 trials (10 experiments) performed with the CT-SDR. These trajectories were mapped out using the following two equations:

$$x = r_{avg}\ sin(\theta) \qquad (2)$$
$$y = r_{avg}\ (cos(\theta) - 1)$$

where r_{avg} is the average value of the measured midline radius of curvature r for three trials performed for each experiment and measured from the Sawbone cross sections seen in Fig. 5-C, and θ was found from the arc length of the NiTi steering cannula ($s \in \{0 - L\}$, where L is the length NiTi cannula) and the measured r_{avg} as follows (3).

$$\theta = \frac{s}{r_{avg}} \qquad (3)$$

A list of trajectory positions (x, y) was then generated for root mean square (RMS) error calculation and plotting (Fig. 9) with θ values between 0 and maximum θ with steps of 0.01 radian. The Euclidean distance between each position on the midline arclength and its corresponding desired position for each θ

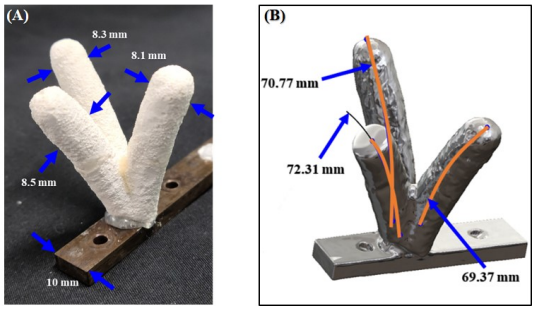

Fig. 7: The plaster (A) and laser scanned (B) representations and measurements of the drilled out-of-axial-plane Branch J-shape drilling tunnels. The plaster model was attached to a reference holder with a known width so accurate measurements could be taken of the path trajectories. The center of cross sections were used to measure the radius of curvature for the entire path. The three J-shape trajectories shown were drilled with the ball end mill tool from a single entry point with the 71.1 mm radius NiTi tube. Radius of curvature of the drilling trajectories and the diameters of the branches are shown in mm.

value was used to perform the RMS shape error calculation for the trajectory. For these experiments, the average of the drilling force magnitudes as well as the components of the drilling force were also recorded and shown in Fig. 10 and Fig. 12, respectively.

2) Out-of-Axial-Plane Branch J-shape Drilling tunnels from a Single Entry Point: In addition to the performed single J-shape axial plane drilling trajectories, experiments were conducted to determine the abilities of the CT-SDR in drilling multiple out-of-axial-plane J-shape trajectories from a single access point. In this set of experiments, the CT-SDR was used to enter from one hole and then drill through multiple different planes (e.g., across the perpendicular sagittal plane) other than the axial plane shown in Fig. 1. This feature enables reaching multiple locations within the vertebral body after entering through the same entry point thus minimizing the extra unnecessary removal of bone and weakening the structure of the vertebral body [13]. Based on the results obtained in the performed J-shape drilling experiments, this experiment was run with an insertion speed of 0.85 mm/s, rotational speed of 8250 rpm, and with both drilling instruments. To compare the performance of the drilling instruments, we used both tools in the experiments, a focus was placed on the 71.1 mm radius tube, to show longer path lengths. As shown in Fig. 7, we successfully performed a branch cutting experiment with three J-shape trajectories from single entry points.

As the C-arm used in the previous experiments provides 2D images and is unable to create clear and succinct visualization of the 3D directions/depths, the branching paths were filled with plaster (B08XW9ML9P, Amazon) and the Sawbones test samples were treated as a mold. The Sawbones material was then removed to reveal a full visualization of the interior paths. This 3D sample, shown in Fig. 7, allowed us to qualitatively inspect the radius of curvature, length, and smoothness of the drilled trajectories in the laboratory instead of using complex imaging modalities such as CT scans. Additionally,

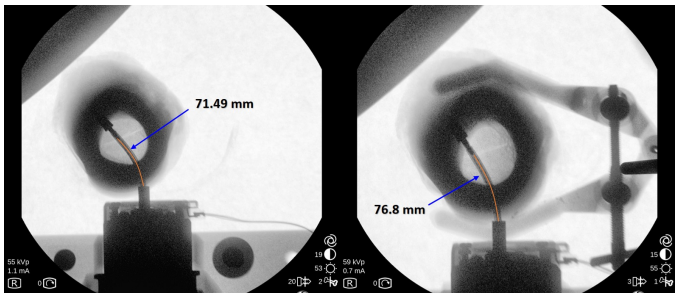

Fig. 8: Representative X-ray images from animal drilling experiments performed with the 71.1 mm NiTi tube. Radius of curvature of the drilling trajectory is shown in mm.

to quantitatively evaluate the performance of the CT-SDR in branch cutting experiment, the plaster was then laser scanned using a handheld and portable 3D scanner (Artec Space Spider, Artec 3D Inc.) and its model exported into 3D CAD software (SolidWorks, Dassault Systèmes) for further analysis. Figure 7 also displays the 3D rendering of the scanned plaster and the performed measured dimensions.

C. Animal Bone Drilling Experiments

To evaluate the CT-SDR in a more realistic drilling environment, we also verified its functionality on animal bones using the setup shown in Fig. 4. For these experiments, similar to [18], we used beef shank of various sizes and followed a similar experimental procedure described in Section III-B to perform 10 different drilling experiments through the bone marrow. It is worth noting that in these experiments, we are simulating a realistic surgical workflow in which a surgeon first creates a pilot hole through the cortical bone and, particularly, the pedicle and then introduces the drill to the vertebral body (see Fig. 1). For performing each test, the CT-SDR was aligned to drill across the horizontal plane for optimal viewing by the X-ray, the specimen was secured to the six axis force/torque load cell supported platform, and the drill actuated through the specimen using the 0.85 mm/s insertion speed and 8250 rpm drilling speed. To confirm the robot was behaving as expected, the C-arm was used to monitor the live drilling trajectory throughout the drilling process, as shown in Fig. 4 and Fig. 8. To thoroughly evaluate the robustness, repeatability, and performance of the CT-SDR in drilling accurate pre-planned trajectories (determined by the heat treated shape of NiTi tubes) and the interaction force during the drilling procedure, 5 tests were run with each of the 71.1 mm and 35.7 mm radii steering cannula, totalling 10 different experiments. In addition, Fig. 11 illustrates the average magnitude of the measured drilling force using both the 35.7 mm and 71.1 mm radii cannula throughout the experiments captured by the force/torque load cell, along with X-ray views of three tests performed with the 35.7 mm radius cannula. Of note, since the length of the drilled path was limited by the bone geometry and size, the length and time of measurements are different for the performed experiments.

IV. Discussion

As described, to thoroughly evaluate the performance of the CT-SDR in a realistic surgical setting, we were mainly

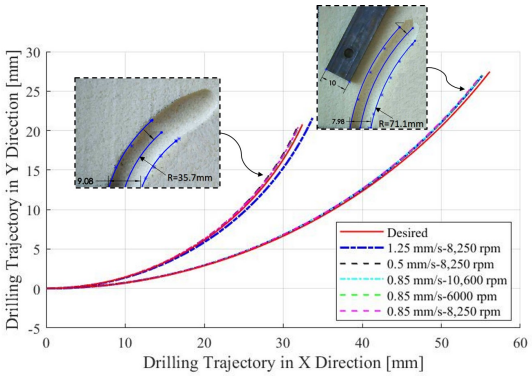

Fig. 9: Comparison of the average measured and the desired drilling trajectories of the 30 trials (10 experiments each repeated three times) for different CT-SDR settings performed on sawbone samples using both 71.1 mm and 35.7 mm radii steering cannula.

interested in three different evaluation criteria including (1) the time it took for the CT-SDR to progress through the entire path and create a J-shape drilling trajectory, (2) the repeatability and consistency of the drilled path as compared to the results reported in the previous literature (i.e., [12], [13], [16], [17]), and (3) the drilling force exerted by the CT-SDR on the specimen during drilling procedure in Sawbone and animal bone samples. The following sections discuss in detail the obtained results.

1) Drilling Time: In our performed experiments, the time to drill the complete path began when the insertion of the drill started, right before it touched the sample, and ended when the drill was turned off and removed from the test sample. As opposed to the results reported in [13], this test was performed to ensure that the use of CT-SDR in a surgical procedure does not add a significant amount of drilling time compared with the currently used rigid drilling instruments. As summarized in Table I, the faster insertion times were generated with the fastest insertion speed of 1.25 mm/s. On average, a full J-shape path drilled with the 71.1 mm radius NiTi tube took 43.7 seconds. Also, as reported in Table II, for the CT-SDR made of the NiTi tube with 35.7 mm radius of curvature required 35 seconds on average to fully drill a path through the Sawbone samples. Of note, the NiTi tube with smaller radius had a smaller path length (i.e., 41 mm versus 65 mm for the tube with the 71.1 mm radius) which led to the difference in these two times. The significance of these times comes from the comparisons to previously-made similar instruments in the literature. For instance, the proposed CT-SDR is more than 10 times faster than the drill designed by Alambeigi et al. in [13]. Moreover, although the proposed handheld curved drilling device presented by Ma et al. [17] does not directly report the drilling time and trajectory length, the maximum utilized feed velocity without buckling, as the direct measure of drilling speed, was 0.4 mm/s, which is >3 times slower than the maximum insertion speed used in our experiments (i.e., 1.25 mm/s). The study performed by Wang et al. [16] also does not report any deep drilling experiments within the hard tissue samples to compare the performance of their system with the proposed CT-SDR. Previous works have shown that other flexible drilling robots lack adequate structural stiffness and will buckle when higher insertion speeds are used [15], [17]; however, the NiTi tubes utilized in the CT-SDR demonstrate adequate rigidity despite being flexible enough to drill through high bending curvatures. Therefore, this feature mitigates the risk of buckling and allows for a safe and faster drilling procedure.

2) Repeatability and Consistency of J-shape Tunnels: The repeatability and consistency of the CT-SDR's drilling performance on the J-shape drilled paths was studied by analyzing the cross sections of the drilled trajectories after experimentation (shown in Fig. 5). As shown in Table II, the high insertion speed of 1.25 mm/s caused an increase in the lateral force on the drill tip during the procedure creating a slight deformation of the NiTi and, therefore, a larger error in the final trajectory (i.e., 4.1% at 1.25 mm/s with 8250 rpm). This error was mitigated when the insertion speed was decreased slightly (i.e., 1.57% at 0.85 mm/s with 8250 rpm), and almost completely removed in this series of tests when the drill tip rotational speed was also increased (i.e., 0.14% at 0.85 mm/s with 10600 rpm). As can be observed in Fig. 9, among the performed experiments, the maximum tip position error between the measured and the desired trajectories was less than 1.5 mm. On average, the trajectory RMS shape errors between the calculated average trajectories using (2) and the generated desired trajectories were 0.4782 mm for the 71.1 mm radius and 0.3056 mm for the 35.7 mm radius steering cannula. The lateral forces were less extreme in the case of the NiTi tube with the larger radius and as displayed in Table I the tests all resulted in very similar and highly accurate path trajectories with 1.7-2.15% error. When changing to the ball nose end mill, the paths cut by the CT-SDR were very similar to the cuts with the oval head bur (i.e., an average error of 3.0%). Of note, this feature demonstrates the independence of the drilling performance to the drill bit geometry.

As shown in Fig. 5 and Fig. 7, inspection of the cross-section of the drilled samples and the 3D plaster models clearly display the smooth and identical surfaces for the curved single and multiple branched J-shape trajectories drilled by the CT-SDR. The values shown in Fig. 7 indicate an average radius of curvature of 70.8 mm, which shows only a 2% difference from the actual value of the cannula's curvature. This result clearly confirms the repeatability and consistency of the CT-SDR J-Shape and branch drilling performance independent of the steering cannula's cutting plane. Figure 7 also shows the measured width of the cut tunnels using the ball nose end mill and the oval head bur with an average width of 8.3 mm and 7.83 mm, respectively. Figure 8 also shows exemplary measured drilling trajectories in animal bone samples obtained using X-ray images. These images demonstrate an average error of 3.43% when comparing the drilling trajectories with the average mid-line of the steering cannula's curvature. Of note, this value is within the approximate ranges of errors measured in the performed Sawbone tests.

As opposed to the created smooth and repeatable J-shape curved trajectories using the CT-STR, the proposed steerable drilling system by Wang et al. [16] produced multi-segment linear trajectories that creates a sharp angle and an unnecessary

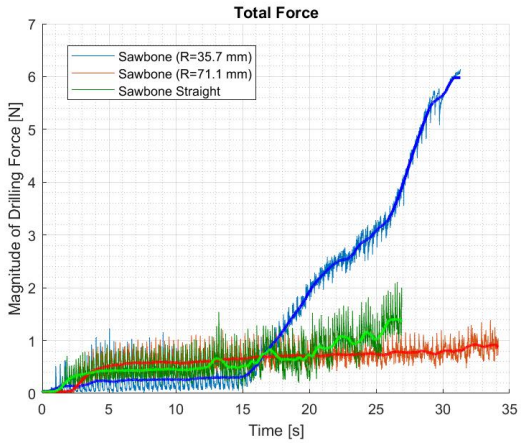

Fig. 10: Average magnitude of the measured drilling force throughout the drilling procedure on Sawbone samples captured by the force/torque load cell. Plot demonstrates the average measured forces during two repeated trials while drilling in a straight trajectory and two J-shape trajectories represented by R= 35.7 mm and R= 71.1 mm radii of curvature.

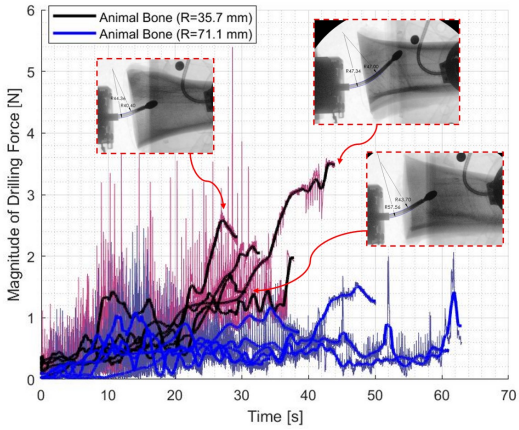

Fig. 11: Total magnitude of the measured drilling force throughout the drilling procedure on animal bone samples captured by the force/torque load cell in the performed 10 experiments with both the 35.7 mm and 71.1 mm radii cannula. X-ray images are shown of three exemplary cases drilled with the 35.7 mm cannula along with trajectory measurements of their resulting curvatures. Of note, since the length of the drilled path was limited by the bone samples' geometry and size, the length and time of measurements are different for the performed experiments.

cavity to rotate the head of the drilling wrist to change the drilling direction. Of note, due to this non-smooth drilling trajectory, such tunnels cannot be used for spinal fixation procedure with a pedicle screw. Similarly, due to the underactuation and lack of adequate stiffness of the proposed continuum manipulator by Alambeigi et al. [13], [17], as the curved drilling robot, these devices are also unable to create a smooth curved drilling trajectory in a drilling environment and demand active and real-time control of tendons' tensions to create sufficient stiffness for the drilling robot. Nevertheless, the proposed CT-SDR creates truly-smooth curved trajectories to provide a smooth path for placement of flexible surgical implants (e.g., flexible screws [12]) or further instrumentation in high BMD regions of the vertebral body. Further, this qualitative comparison together with the quantitative experimental results clearly demonstrate that the two different drill bits used in the experiments have minimal effect on the drilling process and outcome as a whole, and were both viable options for the proposed CT-SDR. The performed experiments also clearly demonstrated the intuitive and easy-to-steer controlling procedure of the proposed CT-SDR to create smooth and repeatable drilling trajectories in which the bending and insertion DoFs are decoupled using the pre-defined bending curvature of the heat treated NiTi tubes. As described, to actively steer the CT-SDR along a planned trajectory, we solely controlled the insertion speed as opposed to the robotic systems proposed in [13], [16], [17], which required active and simultaneous control of these DoFs.

3) Drilling Force: Figure 10 illustrates the average magnitude of the drilling forces in two repeated trials for each of the following CT-SDR configurations: straight drilling, with the 35.7 mm steering cannula, and with the 71.1 mm steering cannula, as captured by the force/torque load cell (with frequency of 1 kHz) throughout the experiments performed on Sawbone samples. Also, this figure shows both measured and smoothed averaged forces using the *smooth* function in MATLAB (MATLAB, MathWorks) with a span of 100 during drilling in a straight trajectory and two curved trajectories represented by R = 35.7 mm and R = 71.1 mm radii of curvature. As can be observed, the magnitude of the measured drilling forces depends on the curvature of the drilling trajectory and the hardness of the drilling material. For the straight and R= 71.1 mm drilled trajectory in Sawbone samples, the drilling force through the experiment is almost below 1 N whereas this value is dramatically increased (with maximum 7 N) for the drilled trajectory with the higher curvature (i.e., R = 35.7 mm) in Sawbone samples. Figure 11 shows the total magnitude of force felt by the bone samples during the CT-SDR drilling for 5 tests run with the 35.7 mm radius cannula and 5 tests performed with the 71.1 mm radius cannula (these forces were smoothed in a similar manner to those shown in Fig. 10). The highest force peaked around 3.5 N for the 35.7 mm radius trajectory, at the very end of the drilling path. Additionally, Fig. 11 illustrates the CT-SDR's shape and the drilling trajectory when reading this force in the accompanying X-ray images. Of note, the maximum values for each of the 35.7 mm tests were greater than those found in any of the 71.1 mm tests. For all of the tests performed on the bone specimens, the observed trends are similar to the ones seen in the Sawbone samples. For the clarity of presentation, Figure 12 only shows the components of the measured and smoothed forces in two exemplary cases during animal bone drilling performed with the 35.7 mm radius of curvature. Of note, the measured drilling forces (both components and magnitude) are well within the measured ranges reported in the literature (e.g., [13], [15], [18]).

V. Conclusion and Future Work

Toward improving quality of spinal fixation in osteoporotic vertebrae, we proposed a CT-SDR to address the contradictory

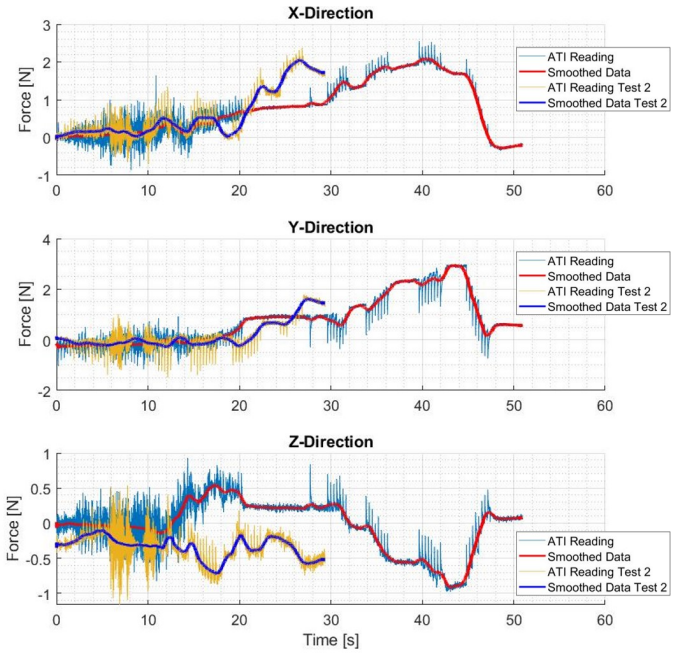

Fig. 12: Exemplary components of the measured and smoothed forces during two tests of animal bone drilling performed with the 35.7 mm radius of curvature. Of note, since the length of the drilled path was limited by the bone geometry and size, the length and time of measurements are different for the performed experiments.

requirements of the adequate structural stiffness and dexterity needed for a steerable surgical drill when performing minimally invasive procedures on hard tissues. The proposed design was thoroughly evaluated with two different steering cannulas and flexible instruments and via an easy-to-steer control algorithm. Results successfully demonstrated the outperformance of the proposed CT-SDR as compared with the existing flexible drilling devices in the literature by (i) repeatedly and consistently creating single and multiple J-shape drilling trajectories in 30 different experiments on Sawbone samples, which mostly accomplished under 60 seconds with an error between 0.14-4.1% between the measured radii of curvature and the planned trajectories; (ii) obtaining average RMS shape errors of 0.3056 mm and 0.4782 mm for the 35.7 mm and 71.1 mm drilled trajectories, respectively; and (iii) achieving the maximum tip position error of 1.5 mm across all performed experiments. Additionally, when performing 10 different drilling experiments through animal bone specimens, similar to the trials performed on Sawbone samples, the CT-SDR could recreate the planned curved trajectories, as shown in Fig. 11, while creating drilling forces that were well within acceptable ranges reported in the previous literature, without requiring an on-the-fly control algorithm for the bending DoF (e.g., [13], [15], [18]). In the future, we will expand the capabilities of the proposed CT-SDR in drilling S-shape trajectories with different curvatures by using two or more NiTi tubes. For such a CT-SDR, we will develop mathematical models that considers the impact of drilling forces on the deformation behavior of NiTi tubes and also will implement control algorithms enabling on-the-fly control and curvature correction of tubes during the drilling procedure. Moreover, we also explore the possibilities that will come from adding water and/or air to the system to irrigate the drilled tunnel for simultaneous removal of the drilled bone and the heat generated during the drilling process. In addition, we will fabricate different flexible instruments for creating threads for implanting bendable pedicle screws (similar to the ones proposed in [11], [12]) inside the drilled curved trajectories as well as instruments for tumor removal and/or biopsy. We will also explore the functionality of the CT-SDR in drilling cadaver specimens.

REFERENCES

[1] O. of the Surgeon General (US *et al.*, "Bone health and osteoporosis: a report of the surgeon general," 2004.

[2] J. A. Kanis, L. J. Melton III, C. Christiansen, C. C. Johnston, and N. Khaltaev, "The diagnosis of osteoporosis," *Journal of bone and mineral research*, vol. 9, no. 8, pp. 1137–1141, 1994.

[3] N. C. Wright, A. C. Looker, K. G. Saag, J. R. Curtis, E. S. Delzell, S. Randall, and B. Dawson-Hughes, "The recent prevalence of osteoporosis and low bone mass in the united states based on bone mineral density at the femoral neck or lumbar spine," *Journal of Bone and Mineral Research*, vol. 29, no. 11, pp. 2520–2526, 2014.

[4] R. Burge, B. Dawson-Hughes, D. H. Solomon, J. B. Wong, A. King, and A. Tosteson, "Incidence and economic burden of osteoporosis-related fractures in the united states, 2005–2025," *Journal of bone and mineral research*, vol. 22, no. 3, pp. 465–475, 2007.

[5] O. Johnell and J. Kanis, "An estimate of the worldwide prevalence and disability associated with osteoporotic fractures," *Osteoporosis international*, vol. 17, no. 12, pp. 1726–1733, 2006.

[6] C. M. Klotzbuecher, P. D. Ross, P. B. Landsman, T. A. Abbott III, and M. Berger, "Patients with prior fractures have an increased risk of future fractures: a summary of the literature and statistical synthesis," *Journal of bone and mineral research*, vol. 15, no. 4, pp. 721–739, 2000.

[7] R. Wittenberg, M. Shea, D. Swartz, K. Lee, A. White 3rd, and W. Hayes, "Importance of bone mineral density in instrumented spine fusions." *Spine*, vol. 16, no. 6, pp. 647–652, 1991.

[8] K. Okuyama, K. Sato, E. Abe, H. Inaba, Y. Shimada, and H. Murai, "Stability of transpedicle screwing for the osteoporotic spine. an in vitro study of the mechanical stability." *Spine*, vol. 18, no. 15, pp. 2240–2245, 1993.

[9] L. Weiser, G. Huber, K. Sellenschloh, L. Viezens, K. Püschel, M. M. Morlock, and W. Lehmann, "Insufficient stability of pedicle screws in osteoporotic vertebrae: biomechanical correlation of bone mineral density and pedicle screw fixation strength," *European Spine Journal*, vol. 26, no. 11, pp. 2891–2897, 2017.

[10] C. L. Goldstein, D. S. Brodke, and T. J. Choma, "Surgical management of spinal conditions in the elderly osteoporotic spine," *Neurosurgery*, vol. 77, no. suppl_1, pp. S98–S107, 2015.

[11] F. Alambeigi, M. Bakhtiarinejad, A. Azizi, R. Hegeman, I. Iordachita, H. Khanuja, and M. Armand, "Inroads toward robot-assisted internal fixation of bone fractures using a bendable medical screw and the curved drilling technique," in *2018 7th IEEE International Conference on Biomedical Robotics and Biomechatronics (Biorob)*. IEEE, 2018, pp. 595–600.

[12] F. Alambeigi, M. Bakhtiarinejad, S. Sefati, R. Hegeman, I. Iordachita, H. Khanuja, and M. Armand, "On the use of a continuum manipulator and a bendable medical screw for minimally invasive interventions in orthopedic surgery," *IEEE transactions on medical robotics and bionics*, vol. 1, no. 1, pp. 14–21, 2019.

[13] F. Alambeigi, Y. Wang, S. Sefati, C. Gao, R. J. Murphy, I. Iordachita, R. H. Taylor, H. Khanuja, and M. Armand, "A curved-drilling approach in core decompression of the femoral head osteonecrosis using a continuum manipulator," *IEEE Robotics and Automation Letters*, vol. 2, no. 3, pp. 1480–1487, 2017.

[14] H. Alfalahi, F. Renda, and C. Stefanini, "Concentric tube robots for minimally invasive surgery: Current applications and future opportunities," *IEEE Transactions on Medical Robotics and Bionics*, vol. 2, no. 3, pp. 410–424, 2020.

[15] F. Alambeigi, Y. Wang, R. J. Murphy, I. Iordachita, and M. Armand, "Toward robot-assisted hard osteolytic lesion treatment using a continuum manipulator," in *2016 38th Annual International Conference of the IEEE Engineering in Medicine and Biology Society (EMBC)*. IEEE, 2016, pp. 5103–5106.

[16] Y. Wang, H.-W. Yip, H. Zheng, H. Lin, R. Taylor, and K. W. S. Au, "Design and experimental validation of a miniaturized robotic tendon-driven articulated surgical drill for enhancing distal dexterity in minimally invasive spine fusion," *IEEE/ASME Transactions on Mechatronics*, 2021.

[17] J. H. Ma, S. Sefati, R. H. Taylor, and M. Armand, "An active steering hand-held robotic system for minimally invasive orthopaedic surgery using a continuum manipulator," *IEEE Robotics and Automation Letters*, vol. 6, no. 2, pp. 1622–1629, 2021.

[18] Y. Wang, H. Zheng, R. H. Taylor, and K. W. S. Au, "A handheld steerable surgical drill with a novel miniaturized articulated joint module for dexterous confined-space bone work," *IEEE Transactions on Biomedical Engineering*, pp. 1–1, 2022.

[19] P. E. Dupont, J. Lock, B. Itkowitz, and E. Butler, "Design and control of concentric-tube robots," *IEEE Transactions on Robotics*, vol. 26, no. 2, pp. 209–225, 2009.

[20] R. J. Webster III and B. A. Jones, "Design and kinematic modeling of constant curvature continuum robots: A review," *The International Journal of Robotics Research*, vol. 29, no. 13, pp. 1661–1683, 2010.

[21] J. Burgner-Kahrs, D. C. Rucker, and H. Choset, "Continuum robots for medical applications: A survey," *IEEE Transactions on Robotics*, vol. 31, no. 6, pp. 1261–1280, 2015.

[22] A. W. Mahoney, H. B. Gilbert, and R. J. Webster III, "A review of concentric tube robots: modeling, control, design, planning, and sensing," *The Encyclopedia of Medical Robotics: Volume 1 Minimally Invasive Surgical Robotics*, pp. 181–202, 2019.

[23] P. E. Dupont, B. J. Nelson, M. Goldfarb, B. Hannaford, A. Menciassi, M. K. O'Malley, N. Simaan, P. Valdastri, and G.-Z. Yang, "A decade retrospective of medical robotics research from 2010 to 2020," *Science Robotics*, vol. 6, no. 60, p. eabi8017, 2021.

[24] P. E. Dupont, N. Simaan, H. Choset, and C. Rucker, "Continuum robots for medical interventions," *Proceedings of the IEEE*, vol. 110, no. 7, pp. 847–870, 2022.

[25] H. B. Gilbert, D. C. Rucker, and R. J. Webster III, "Concentric tube robots: The state of the art and future directions," in *Robotics Research: The 16th International Symposium ISRR*. Springer, 2016, pp. 253–269.

[26] Z. Mitros, S. H. Sadati, R. Henry, L. Da Cruz, and C. Bergeles, "From theoretical work to clinical translation: Progress in concentric tube robots," *Annual Review of Control, Robotics, and Autonomous Systems*, vol. 5, pp. 335–359, 2022.

[27] M. Drexel, G. Selvaduray, and A. Pelton, *The effects of cold work and heat treatment on the properties of nitinol wire*, 2007, vol. 42665.

[28] R. J. Webster, J. M. Romano, and N. J. Cowan, "Mechanics of precurved-tube continuum robots," *IEEE Transactions on Robotics*, vol. 25, no. 1, p. 67–78, 2009.

[29] G. F. SOLITRO, K. WHITLOCK, F. AMIROUCHE, A. I. MEHTA, and A. MCDONNELL, "Currently adopted criteria for pedicle screw diameter selection," *International Journal of Spine Surgery*, vol. 13, no. 2, p. 132–145, 2019.

[30] M. R. ZINDRICK, L. L. WILTSE, E. H. WIDELL, J. C. THOMAS, W. R. HOLLAND, B. T. FIELD, and C. W. SPENCER, "A biomechanical study of intrapeduncular screw fixation in the lumbosacral spine," *Clinical Orthopaedics and Related Research*, vol. 203, no. amp;NA;, 1986.

[31] D. Hodgson, "Fabrication, heat treatment and joining of nitinol components," in *SMST-2000, Proc. Int. Conf. on Shape Memory and Superelastic Technologies*, 2001, pp. 11–24.

[32] A. Çetin and D. A. Bircan, "Experimental investigation of pull-out performance of pedicle screws at different polyurethane (pu) foam densities," *Proceedings of the Institution of Mechanical Engineers, Part H: Journal of Engineering in Medicine*, vol. 235, no. 6, pp. 709–716, 2021.